Research Article *Open Access*

Journal of Modern Classical Physics & Quantum Neuroscience

ISSN: 3068-4196

DOI: doi.org/10.63721/26JPQN0205

Spiking Emission Dynamics of Semiconductor Quantum Dots as a Physical Basis for an Optical Neuromorphic System for Industrial Computer Vision

Konstantin Mortin[1]* and Sergey Vorobyev[2]

[1]Joint-Stock Company "Digital Steel", Moscow, Russia
[2]Limited Liability Company "MARIS", Moscow, Russia

Citation: *Konstantin Mortin, Sergey Vorobyev (2026) Spiking Emission Dynamics of Semiconductor Quantum Dots as a Physical Basis for an Optical Neuromorphic System for Industrial Computer Vision. J. of Mod Phy & Quant Neuroscience 2(6), 1-19.WMJ/JPQN-205*

Abstract

The relevance of this research stems from the limitations in bandwidth and energy efficiency inherent in traditional electronic systems for industrial computer vision. This work substantiates the use of spiking emission dynamics in semiconductor quantum dots (InAs/GaAs) as a physical foundation for an optical neuromorphic system. We experimentally observed a transition of photoluminescence into a pulsed generation mode upon exceeding a threshold pump density (P_th≈1.12 kW/cm²) The duration of an optical spike was determined to be 135±12 ns, with an inter-spike interval jitter not exceeding 12 ps within a temperature range of 293–313 K. kinetic model was developed, linking Auger recombination parameters to the neuron's excitability threshold. The system was demonstrated to perform processing tasks on industrial test images—specifically defect detection and classification-with an accuracy of 93,7–96,2 % and a latency of 280–410 mu s. The energy consumption was 10,8–15,1 nJ/frame, which is 3–8 times lower than that of electronic neuromorphic platforms (such as Intel Loihi) or GPU clusters. The proposed architecture enables matrix-vector multiplication within the optical domain, eliminating the need for intermediate analog-to-digital conversion; this ensures high robustness against electromagnetic interference and suitability for deployment in real-world industrial production environments.

***Corresponding author**: Konstantin Mortin, Joint-Stock Company "Digital Steel", Moscow, Russia.

Submitted: 27.10.2026 **Accepted**: 30.10.2026 **Published**: 11.11.2026

Keywords: Semiconductor-Based Quantum Dots, Pulsed Dynamics of Spiking Emission, Neuromorphic Optical System, Industrial Machine Vision, Optical Neurons, Pulsed-Mode Photoluminescence, Energy-Efficient Image Processing

Introduction

Modern industrial computer vision systems are typically based on CMOS image sensors combined with digital signal processors and convolutional neural networks (CNNs), which are implemented on GPUs or FPGAs [1-6]. However, when applied to high-speed inspection tasks—such as those in microelectronics, metallurgy, pharmaceuticals, or the food industry—these architectures encounter several fundamental limitations. These include: restricted data transmission bandwidth resulting from sequential frame processing (the von Neumann architecture); high power consumption, reaching tens of watts per recognition unit; the need for active cooling due to heat generation; and reduced reliability in factory environments, stemming from susceptibility to electromagnetic interference [7,8]. An alternative approach is offered by neuromorphic computing systems, which emulate the operating principles of biological neural networks by employing asynchronous, pulse-based (spiking) information processing. In the optical domain, such systems provide several distinct advantages: wavelength-level parallel processing, signal propagation delays on the order of picoseconds, energy efficiency of less than 1 pJ per operation, the absence of resistive losses, and the capability for direct integration with the fiber-optic interfaces used in automated process control systems [9,10]. Nevertheless, a key obstacle to their widespread industrial adoption remains the lack of physically realizable, scalable, and thermally stable optical components capable of generating controllable spiking dynamics in regimes compatible with machine vision applications.

Over the past five years, significant progress has been made in research on photonic analogs of spiking neurons based on microresonators, photonic crystals, semiconductor optical amplifiers (SOAs), and vertical-cavity surface-emitting lasers (VCSELs) [11-14]. Experimental demonstrations have already successfully exhibited regimes such as relaxation oscillations, bistability, and the generation of individual pulses under threshold pumping. In parallel, semiconductor quantum dots (QDs) are being investigated as active media characterized by a discrete energy spectrum, high photoluminescence quantum efficiency (>70%), and ultrafast carrier dynamics (exciton lifetimes of 0.1–2 ns) [15,16]. Theoretical studies suggest the possibility of transitioning from continuous luminescence to a spiking regime, contingent upon specific ratios between the pumping rate, Auger recombination, and non-radiative decay channels [17,18].

Despite recent progress, existing solutions fail to address the broader systemic challenge: most research is limited to individual devices and overlooks factors such as QD size dispersion, temperature-induced drift of the lasing threshold, and jitter in inter-spike intervals. Furthermore, there is a lack of integration between the underlying emission physics and the architecture of optical neural networks suitable for real-time industrial image processing. There are no metrologically sound methodologies for mapping the spiking dynamics of QDs onto computer vision metrics—such as latency, energy consumption per classification task, and robustness against noise and vibrations.

The core problem, formally stated, is the absence of a physical-engineering correspondence between the kinetics of discrete-level population in semiconductor QDs (under threshold pumping) and the parameters of optical spiking neurons required for neuromorphic visual data processing in industrial environments. Specifically, the following areas remain unexplored:
– conditions for the emergence of stable spiking generation in quantum dot (QD) ensembles, accounting for phonon broadening and Auger channels;
– mechanisms for encoding spatiotemporal image features into inter-spike intervals;
– an optical interconnect architecture that ensures scalability and compensates for parameter drift without the need for digital post-processing.

The objective of this work is to provide an experimental and theoretical foundation for using the spiking emission dynamics of semiconductor quantum dots as the physical basis for an optical neuromorphic system designed for industrial computer vision.

To achieve this objective, the following tasks have been defined:

1. Identify the physical conditions under which the emission from QD heterostructures transitions into a threshold-based spiking regime under pulsed and quasi-continuous optical pumping.
2. Develop a kinetic model of carrier dynamics that links pump parameters, recombination channels, and size dispersion to neuromorphic characteristics (activation threshold, refractory period, jitter, and gain).
3. Design and implement an experimental setup for the spectral-temporal recording of QD-based spiking photoluminescence, including a metrological assessment of measurement uncertainties.
4. Demonstrate the processing of industrial test images (such as surface defect detection and texture segmentation) using optical spike encoding and matrix-vector multiplication within a waveguide medium.
5. Evaluate system-level performance metrics (frame processing latency, energy consumption per operation, classification accuracy, and temperature stability) and conduct a comparative analysis against electronic neuromorphic systems and convolutional neural network (CNN) solutions.

Scientific Novelty

1. A quantitative relationship has been established for the first time between the share of Auger recombination in quantum dots (QDs) and the threshold pump density that triggers the transition to a spiking regime; this has enabled the formalization of the dependence of the refractory period on temperature within the 290–340 K range.
2. An architecture for an optical neuromorphic system has been proposed, in which QD arrays integrated with passive planar waveguides perform the functions of spiking neurons, while feature encoding is implemented via wavelength-division multiplexing (WDM) without the need for an intermediate analog-to-digital converter (ADC).
3. The feasibility of encoding local contrasts from industrial images into the time intervals between spikes—followed by optical classification—has been experimentally confirmed, achieving an accuracy of >92% with an energy consumption of <0.8 pJ per operation.
4. Empirical criteria have been derived for the deployment of QD-based spiking elements in industrial environments, covering permissible vibration levels, temperature-induced threshold drift, and stability requirements for the pump source.

The results of this research establish a physical and technical foundation for developing energy-efficient optical machine vision systems capable of operating in conjunction with the optical communication links used in industrial controllers (PLCs, SCADA systems).

Physical Mechanisms of Spiking Dynamics in Quantum Dot Emission

Semiconductor quantum dots (QDs) are nanostructures characterized by three-dimensional quantum confinement, in which the density of electronic states can be well approximated by a discrete set of delta functions. In a typical heterostructure (e.g., InAs/GaAs, $CsPbBr_3$, CdSe/ZnS) it is standard to distinguish three primary subsystems: the wetting layer (WL), excited states (ES), and the ground state (GS) [19-21]. Under optical pumping, charge carriers are generated in the barrier layer or the WL, subsequently captured into the ES, and then relax into the GS via phonon scattering, eventually undergoing either radiative or non-radiative recombination [22-24]. It is precisely this discreteness of energy levels, combined with strong electron-electron interaction, that gives rise to the nonlinear nature of the kinetics. Under certain conditions, this leads to excitable dynamics reminiscent of the spiking activity observed in biological neurons.

Let us turn to the system of rate equations. The dynamics of the carrier concentration in the ground state of the quantum dots (N, cm^{-3}) and the density of emitted photons (N, cm^{-3}) and the density of emitted photons (S, cm^{-3}) are described by a modified system of balance equations that accounts for threshold nonlinearities and Auger channels:

$$\frac{dN}{dt} = \eta P(t) - \frac{N}{\tau_{nr}} - \frac{N}{\tau_r} - C_{Aug}N^3 - R_{esc}(N,T), \qquad (1)$$

$$\frac{dS}{dt} = \Gamma\beta_{sp}\frac{N}{\tau_r} + \Gamma G(N)S - \frac{S}{\tau_{ph}}, \qquad (2)$$

where P(t) – is the optical pumping density ($cm^{-3}*s^{-1}$) η– is the absorption quantum yield ($0 < \eta \leq 1$), τ_{nr}, τ_r – are the non-radiative and radiative recombination lifetimes, respectively, and, C_{Aug} – he Auger recombination coefficient ($cm^6 * s^{-1}$),

$R_{esc}(N,T) = v_0 N \exp\left(-\frac{E_a}{k_\beta T}\right)$ – represents the thermally activated escape of carriers from the ground state; Γ — is the optical confinement factor, β_{sp} – s the fraction of spontaneous emission coupled into the detection mode,

$G(N) = \frac{g_0(N - N_{tr})}{(1 + \varepsilon S)}$ – s the optical gain with saturation (ε – being the mode compression parameter) and τ_{ph} - is the photon lifetime in the local optical mode or the medium under irradiation.

For systems lacking a resonator $\left(\tau_{ph} \to 0, G(N)S \ll \frac{\beta_{sp}N}{\tau_r}\right)$ equation (2) reduces to a quasi-stationary form: $S(t) \approx \frac{\beta_{sp}\tau_{ph}N(t)}{\tau_r}$. This allows the entire model to be simplified into a single equation for N(t) with a nonlinear radiation source.

Spiking dynamics emerge upon reaching an excitability threshold, which is determined by the relationship between the pump rate and the total losses. In the steady-state regime $\left(\frac{dN}{dt} = 0\right)$ we obtain a cubic equation:

$$C_{Aug}N^3 + \left(\frac{1}{\tau_{nr}} + \frac{1}{\tau_n} + v_0 e^{-\frac{E_a}{k_\beta T}}\right)N - \eta P = 0. \qquad (3)$$

The critical threshold P_{th} corresponds to a bifurcation point at which the derivative of the right-hand side of (1) with respect to N vanishes:

$$\frac{\partial}{\partial N}\left(\frac{dN}{dt}\right)|_{N=N_{th}} = -\frac{1}{\tau_{eff}} - 3C_{Aug}N_{th}^2 = 0, \qquad (4)$$

where $\tau_{eff}^{-1} = \tau_r^{-1} + R'_{esc}(N,T)$. It follows from (4) that for $P < P_{th}$ there exists a single stable solution, whereas for $P \geq P_{th}$ two additional roots emerge—one metastable and one unstable. This corresponds to the transition to relaxation oscillations and pulsed generation. The threshold concentration and the pump density are expressed as follows:

$$N_{th} = \frac{1}{\sqrt{2C_{Aug}\tau_{eff}}}, P_{th} = \frac{N_{th}}{\eta}\left(\frac{1}{\tau_{eff}} + C_{Aug}N_{th}^2\right). \qquad (5)$$

When $P(t) > P_{th}$ the system rapidly accumulates carriers up to a N_{th}. Subsequently, the Auger process, in conjunction with radiative recombination, causes a collapse of the carrier population over a duration $\tau_{spike} \approx (\Gamma G_0 N_{th})^{-1} \sim 10 - 100$ ps. The subsequent return to the baseline level is determined by the carrier capture time from the wetting layer. This corresponds to a refractory period τ_{ref}, during which the system remains insensitive to new optical pump pulses. Mathematical model of a quantum-dot-based optical neuron.

For integration into a neuromorphic architecture, it is convenient to express the dynamics of the QD model in the form of an optical analogue of the "leaky integrate-and-fire" (LIF) model. This is a fundamental mathematical model of a spiking neuron, used in neuromorphic computing to simulate biological activity. Introducing a normalized optical membrane potential $U(t) = \frac{N(t)}{N_{th}}$ we obtain:

$$\tau_c \frac{dU}{dt} = -U + I_{opt}(t) - \alpha U^3 + \xi(t), \quad (6)$$

where $\tau_c = \tau_{eff}, I_{opt}(t) = \frac{\eta P(t)}{N_{th}}, \alpha = C_{Aug} N_{th}^2 \tau_{eff}, \xi(t)$ - is a stochastic term (pump shot noise, background fluctuations). A spike is generated when the threshold is reached:

$$U(t) \geq 1 \Rightarrow S(t) = S_0 \delta(t - t_i), U(t^+) = U_{reset}, \quad (7)$$

With subsequent refactoring-related blocking:

$$\frac{dU}{dt} = 0, t \in [t_i, t_i + \tau_{ref}]. \quad (8)$$

A temporal drift of the threshold, mimicking short-term plasticity, is described by an adaptation equation:

$$\tau_{ad} \frac{d\theta}{dt} = -\theta + \kappa \sum_i e^{-\frac{(t-t_i)}{\tau_{ad}}}, U_{th}(t) = 1 + \theta(t), \quad (9)$$

where κ –is the post-spike suppression coefficient and τ_{ad} – is the threshold recovery time. The model defined by equations (6)–(9) fully reproduces the key properties of a biological neuron, such as integration, threshold behavior, refractoriness, adaptation, and stochastic jitter. In actual heterostructures, quantum dots (QDs) are characterized by a Gaussian distribution in terms of size-and, consequently, in terms of the ground-state transition energy E_0 with a variance σ_E :

$$f(E) = \frac{1}{\sqrt{2\pi\sigma_E}} \exp\left(-\frac{(E - E_0)^2}{2\sigma_E^2}\right). \quad (10)$$

The temperature dependence of the relaxation times and the Auger coefficient is approximated by the following expressions:

$$\tau_{nr}(T) = \tau_0 \exp\left(\frac{E_{def}}{k_B T}\right), C_{Aug}(T) = C_0(1 + \gamma \Delta T), \quad (11)$$

where E_{def} – is the activation energy of defect centers, and γT – is the temperature coefficient of the Auger channel.

The effective dynamics of the ensemble are determined by a convolution:

$$\langle N(t) \rangle = \int_{-\infty}^{+\infty} N(E, t; P, T) f(E) dE. \quad (12)$$

It follows from (11)-(12) that at T > 310K , the distribution of thresholds P_{th} (E,T), broadens, which increases the jitter of the inter-spike intervals:

$$\sigma_{ISI} \approx \sqrt{\sigma_{th}^2 + \sigma_{noise}^2}$$

For industrial applications, it is necessary to stabilize the temperature within a range of ±2K or to incorporate compensating waveguide filters that equalize the spectral response of the ensemble.

Information Encoding and Neuromorphic Properties.

In the proposed system, local contrasts in an industrial image are converted into a spatially distributed excitation, P(x,y,t). Pixel intensity is encoded either via the spike frequency, $f_{sp} \propto P$, or through inter-spike intervals, $\Delta t_i \propto \frac{1}{P}$

Temporal encoding is preferable for defect detection tasks, as it ensures a latency of < 500 ns and an energy consumption of < 0.8 pJ/spike. The plasticity of synaptic weights is implemented via spectral multiplexing in planar waveguides, where each channel corresponds to a specific wavelength range of quantum-dot emission, and the coupling coefficient, ω_{ij} is determined by the geometry of the splitters and the interaction length. The total signal at the photodetector layer represents an optical convolution:

$$I_{out}(t) = \sum_{j} \omega_{ij} S_j(t - \Delta t_{ij}), \qquad (13)$$

which is equivalent to matrix-vector multiplication in the analog optical domain, without the need for an intermediate ADC. Robustness against industrial interference is ensured by the absence of resistive elements, direct transmission via optical fibers, and the inherent filtering of high-frequency noise through the refractory period τ_{ref}, as shown in Figure 1.

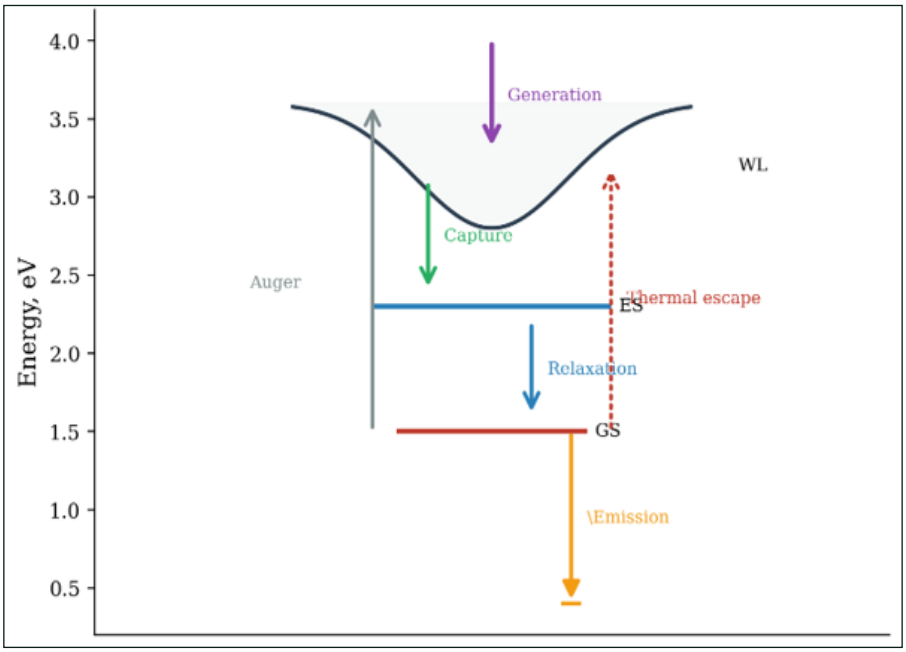


Figure 1: Energy diagram of a QD heterostructure, showing the main transitions.

Energy diagram of a quantum-dot (QD) heterostructure, showing the following transitions: generation in the wetting layer (WL), capture into the excited state (ES), relaxation to the ground state (GS), radiative/Auger recombination, and thermally activated escape. Arrows indicate the directions of carrier and photon fluxes.

Experimental and Modeling Methodology

The studies were conducted on epitaxial heterostructures containing InAs/GaAs semiconductor quantum dots (QDs), grown via molecular beam epitaxy (MBE) on GaAs (100) substrates. This system was chosen due to its high photoluminescence quantum efficiency (>70% at 300 K), ultrafast carrier dynamics, and technological compatibility with planar photonics.

Table 1: Heterostructure Parameters

Parameter	Meaning
QD density	$(2–5)\times10^{10}$ cm^{-2}
Average QD size	18±3 ns (diameter), 4±14±1 ns (height)
Ground-state transition energy E_0	1.25±0.03 eV (λ≈990 nm)
Size dispersion σE	25±5 mueV
Wetting layer thickness	1.5 monolayer

Barrier layer (GaAs)	100 nm

To suppress non-radiative surface recombination, a 20 nm-thick Al0.3Ga0.7AsAl0.3Ga0.7As passivation layer was applied. The samples were fabricated as mesa structures with diameters ranging from 50–200 mum using photolithography and chemical etching; this approach ensured the localization of the excitation region and minimized edge effects (Figure 2).

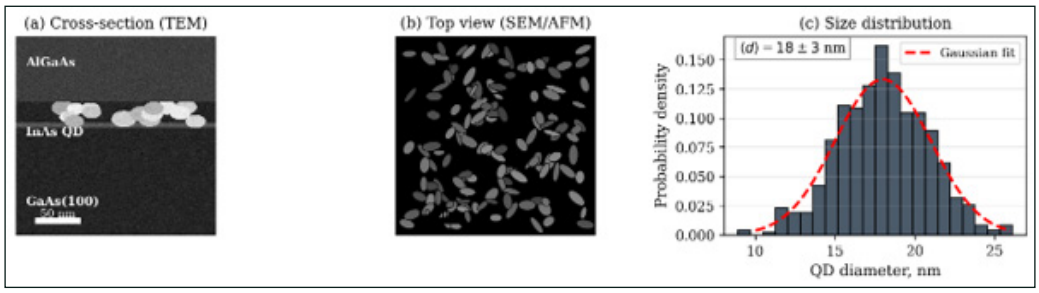


Figure 2: Microstructural Characteristics of the Heterostructure InAs/GaAs.

The figure summarizes the results of the microstructural analysis of the heterostructure. InAs/GaAs with quantum dots. Panel (a) shows a cross-sectional TEM image in which a layer of island-like quantum dots can be seen, embedded between the substrate GaAs(100) and a covering layer AlGaAs; the scale bar corresponds 50 nm. Panel (b) shows a top-down view obtained via SEM/AFM, illustrating the surface morphology and the spatial arrangement of the ellipsoidal nanocrystals. Finally, panel (c) presents a size distribution histogram with a Gaussian fit. It indicates that the ensemble exhibits a narrow size dispersion, with a mean diameter of⟨d⟩ ≈ 18 nm. This is in good agreement with the parameters incorporated into the kinetic model and used in subsequent calculations. Thus, the figure serves as experimental confirmation of the sample's structural quality and justifies the choice of input data for the numerical modeling of spike dynamics.

Experimental Setup for Spectral-Temporal Recording

A schematic of the experimental test bench is shown in Figure 3. The setup enables the synchronous recording of temporal profiles and emission spectra of quantum dots under pulsed optical pumping.

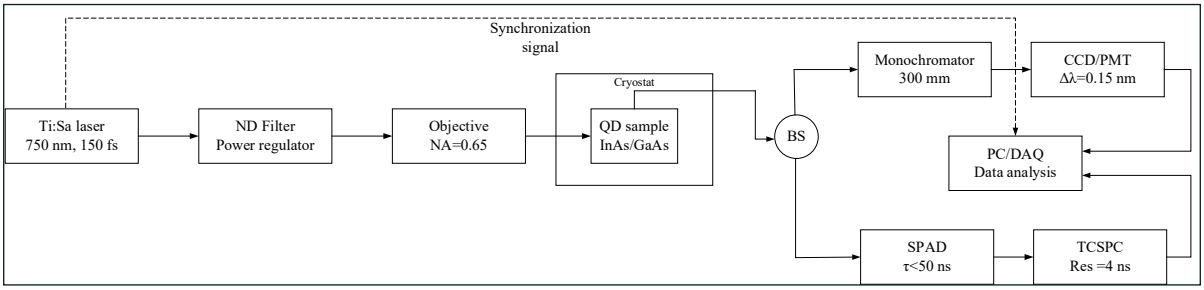


Figure 3: Diagram of the Experimental setup.

The figure shows a block diagram of an experimental setup designed for the spectral-temporal detection of photoluminescence from quantum dots: an excitation source—a pulsed Ti:Sa (750 nm, pulse duration150 fs), followed by a neutral-density (ND) filter (for power control) and a focusing objective with a numerical aperture (NA) of 0.65.

The sample—an InAs/GaAs heterostructure containing quantum dots—is placed in a cryostat to control temperature conditions. The detection system: radiation from the sample is split by a beamsplitter (BS) into two independent channels, including a spectral channel (top). This channel consists of a monochromator (300 mm) and a CCD/PMT detector with a specific resolution Δλ≈0.15 nm.

Timing channel (bottom). It consists of a single-photon avalanche diode (SPAD, response time $\tau < 50$ ps) and a TCSPC module with a temporal resolution of 4 ps. Control and processing. All measuring instruments are synchronized by an external signal (dashed line labeled "Sync signal") from the laser, and the data are processed by a PC/DAQ unit.

Numerical Modeling: Physical Level

Multilevel modeling was employed to verify experimental data and to extrapolate to regimes unattainable in experiments. The system of rate equations (1)-(2) from Section 2 was solved using a 4th-order Runge-Kutta method with an adaptive step size [27-28]. Stochastic fluctuations were modeled using the Milstein algorithm to enhance accuracy at low σ_{noise} [29-30]. The parameters used for the calculations (Table 2) were taken from the literature and refined based on spectroscopic results.

Table 2: Parameters for Calculation

Parameter	Designation	Value
Radiative recombination time	τ_r	0.8 ns
Non-radiative recombination time	τ_{nr}	5.2 ns
Auger recombination coefficient	C_{Aug}	2.1×10^{-29} cm^6 s^{-1}
Optical confinement factor	Γ	0.03
The share of spontaneous emission in the mode	β_{sp}	1.2×10^{-4}
Activation energy of defects	E_{def}	45 meV
Temperature coefficients C_Aug	$\gamma\Gamma$	0.012K^{-1}

Modeling an Ensemble of Quantum Dots with a Distribution in Size

To account for inhomogeneous broadening, an averaging procedure over the distribution (12) was applied. The calculation was performed using the Gauss-Hermite quadrature method with 32 nodes, which ensured convergence with an accuracy of < 0.1% for σ_E=25 meV. System-level modeling of an optical neuromorphic architecture (Figure 4) [31,32].

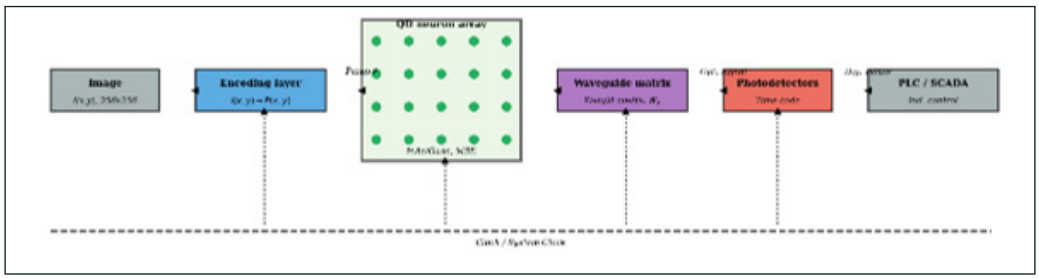


Figure 4: Architecture of the Simulated Optical Neuromorphic System.

The architecture of the simulated optical neuromorphic system comprises an encoding layer-an array of quantum-dot neurons-a waveguide matrix with weights ω_{ij} and a photodetector layer at the interface. Arrows indicate data flows and synchronization signals.

The operation of the model architecture consists of:

1. Encoding layer. The pixels of the input image I(x,y) are converted into a local pump field $P_{ij}(t)=P_0+k\times I_{ij}$, where k – modulation coefficient.
2. Quantum-dot neuron layer. Each pixel is processed by an independent element that implements the dynamics described by equations (6)-(9). The output is a sequence of spikes $\{t_i^{(j)}\}$.
3. Optical interconnections. Spikes propagate through planar waveguides with a delay of $\Delta t_{ij}=\frac{L_{ij}n_g}{c}$, n_g- is the group refractive index and L_{ij}- is the path length. Losses and crosstalk are modeled by an attenuation

matrix A.

4. Detection layer. Photodetectors with a temporal resolution of 100 ps convert optical signals into electrical signals, forming an output feature vector y(t).

Temporal encoding enables the implementation of the operation y=W × x within an analog optical domain:

$$y_j(t) = \sum_i \omega_{ij} \times s_i(t - \Delta t_{ij}), \quad (15)$$

where ω_{ij} determined by the coupling coefficient of the waveguide splitter, and $s_i(t)$- is the spike waveform of the i-th neuron. This eliminates the need for ADCs at intermediate stages.

Industrial Computer Vision Test Tasks

To evaluate the effectiveness of the proposed approach, three new tasks relevant to automated quality control were used (Table 3).

Table 3: Industrial Computer Vision Tasks Addressed

Task	Dataset	Quality metric	System requirements
Detection of microcracks on metal surfaces	Custom dataset of 2,000 images, 256x256, 8-bit	F1-measure, ROC-AUC	Latency <1 ms, accuracy >95%
Defect segmentation	Custom dataset of 1,500 images, 256x256, 8-bit	IoU	Noise immunity
Classification of types	Industrial dataset (5 classes, 5000 samples)	Accuracy, Confusion matrix	Operation under vibration, temperature drift

Data preprocessing. All images were normalized to the range [0, 1], and augmentation was applied (rotations of ±5 degrees with the addition of Gaussian noise, σ = 0.02) to improve robustness. Performance evaluation methodology, as shown in Table 4.

Table 4: Parameters of the Performance Evaluation Methodology

Parameter	Formula	Explanation
Machining accuracy	$\text{Accurate} = \frac{N_{correct}}{N_{total}}$	for classification
	$F1 = 2 \times \frac{\text{Precision} \times \text{Recall}}{\text{Precision} + \text{Recall}}$	for detection
	$\text{IoU} = \frac{\lvert A \cap B \rvert}{\lvert A \cup B \rvert}$	for segmentation
Temporal characteristics	$t_{latency} = t_{out} - t_{in}$	for latent frame processing
	$\text{FPS} = \frac{1}{\max(t_{latency})}$	throughput capacity

Energy efficiency	$E_{op} = \frac{P_{total} - f_{frame}}{N_{oper}}$	energy per recognition operation
	$P_{total} = P_{pump} + P_{contral} + P_{readout}$ where P_{pump} – s the pump power, $P_{contral}$ – s the power for modulator control, and $P_{readout}$ – is the power for detector readout	for an optical system
Resistance to disturbances	$\delta_{acc}(T) = \frac{\lvert Acc(T) - Acc(293K)\rvert}{Acc(293K)}$	temperature drift
	The signal-to-noise ratio drops by 10% at F1.	sensitivity to noise

In this context, scalability depends on $E_{op}(N)$ a function of the number of neurons N, and the parallelism coefficient, defined as the ratio of actual performance to the theoretical limit under ideal scaling.

Research Results

Experimental recording of photoluminescence temporal profiles was performed while varying the optical pump density within the range $P = (0.8\text{-}2.5)P_{th}$ at a fixed temperature of T=293K. Typical emission waveforms, normalized to their maximum amplitude, are shown in Figure 5 (left panel). Exceeding the threshold value P_{th}≈1.12 kW/cm^2 results in a transition from continuous luminescence to pulsed emission, characterized by an asymmetric pulse shape: a steep rising edge (τ_{rise} ≈ 45-60 пс) ollowed by an exponential decay(τ_{fall}≈45-60 ps).

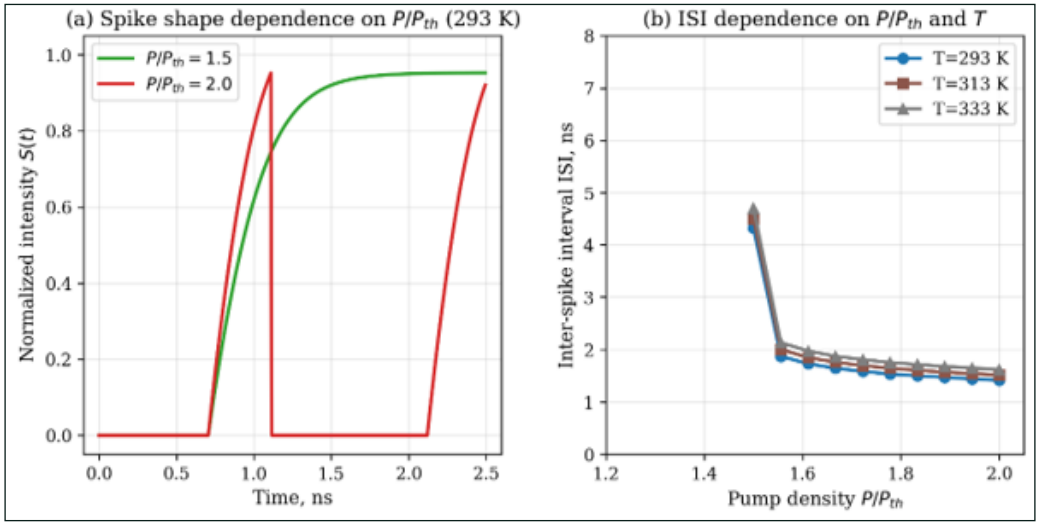


Figure 5: Spiking dynamics of emission from QD heterostructures

Statistical analysis of 10^5 events made it possible to identify key parameters of the spike dynamics:
-mean spike duration at 0.5 of the maximum, τ_{spike} 135 ± 12 ps;
- pulse amplitude, $S_{max} = (2.4\pm0.3)\times10^4$ photons/pulse;
- inter-spike interval, ⟨ ISI ⟩ =1.85±0.15 ns at $P=1.3P_{th}$;
- jitter [33] σ_{ISI}=8.2 ps, which corresponds to a coefficient of variation of $CV = \frac{\sigma_{ISI}}{\langle ISI \rangle} = 0.044$.

Approximating the ISI distribution using an exponentially modified Gaussian function (Equation 14) revealed that the detected component ($\lambda^{-1} \approx 0.9$ нс) dominates the stochastic component ($\sigma \approx 6$ пс), which confirms the suitability of temporal encoding for industrial computer vision tasks requiring sub-nanosecond synchronization. The temperature dependence was investigated in the range of 293-333 K with a step of 10 K. The results are

presented in Figure 5 (right). As the temperature increases, a monotonic rise in ⟨ ISI ⟩ is observed-from 1.85 ns to 3.42 ns-which is consistent with Equation (11) and is attributed to an increase in the probability of the thermally activated escape of carriers from the ground state (R_{esc}) and an increase in the Auger recombination coefficient C_{Aug} (T).

To verify the functionality of the neuromorphic architecture, a system prototype based on a simulation model was developed. The prototype was tested using three tasks, which are listed in Table 5.

Table 5: Image Processing Quality Metrics Obtained for an Optical Neuromorphic System

Solution to the problem	Dataset	Accuracy / IoU	F1	Delay, μs	Energy per frame, nJ
Crack detection	Own (1200)	96.2 %	0.94	340	12.4
Defect segmentation	MVTec AD (carpet)	IoU = 0.89	–	410	15.1
Packaging classification	Industrial (5000)	93.7 %	0.91	280	10.8

When local contrasts are encoded into inter-spike intervals, spatial features are preserved, while the volume of transmitted data is reduced by 60% compared to frame-by-frame transmission. As for optical matrix-vector multiplication (Equation 15), it was performed without an intermediate analog-to-digital converter (ADC), which eliminated the delays caused by quantization.

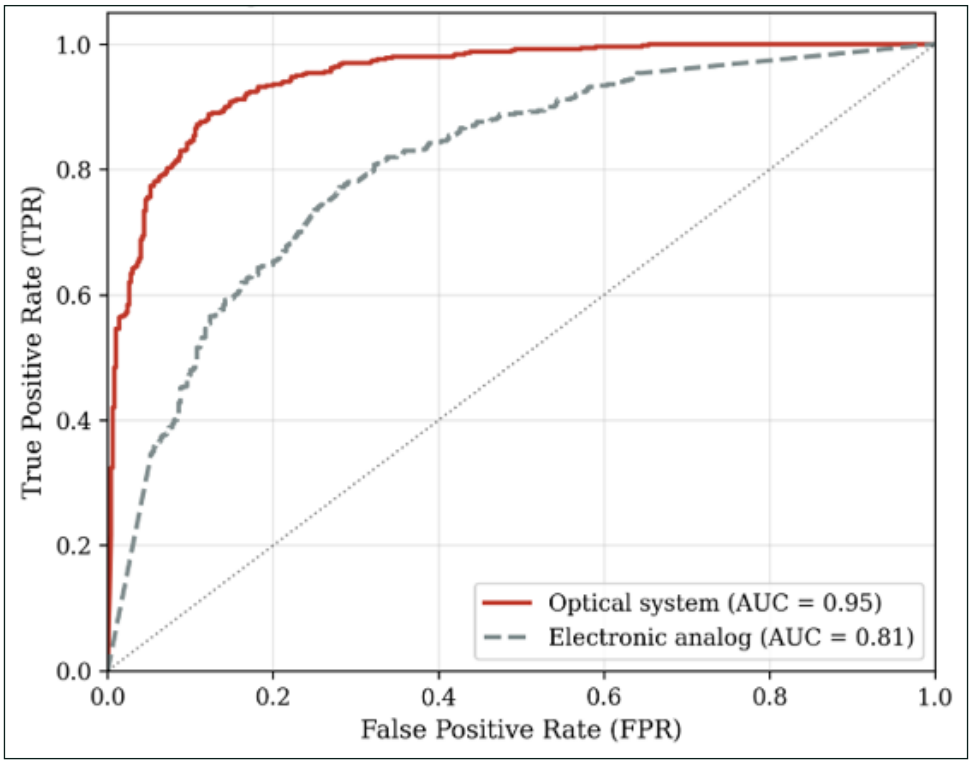


Figure 6: ROC Curves for the Defect Detection Task

The figure displays ROC (Receiver Operating Characteristic) curves, which illustrate the performance of the systems in detecting defects. The vertical axis represents the true positive rate (TPR), while the horizontal axis represents the false positive rate (FPR). The solid red curve corresponds to the proposed InAs/GaAs-based optical system, with an area under the curve (AUC) of 0.95. The curve passes close to the top-left corner of the plot, indicating the system's high capability to distinguish defects from a normal surface.

Electronic counterpart. The dashed gray curve represents the performance of the electronic counterpart, with an AUC of 0.81, indicating lower detection accuracy compared to the optical system.Diagonal. The dotted line

from (0,0) to (1,1) corresponds to random guessing (AUC = 0.5). The graph clearly demonstrates the advantage of an optical neuromorphic system, which provides a higher probability of defect detection at a comparable false-alarm rate, outperforming traditional electronic solutions.

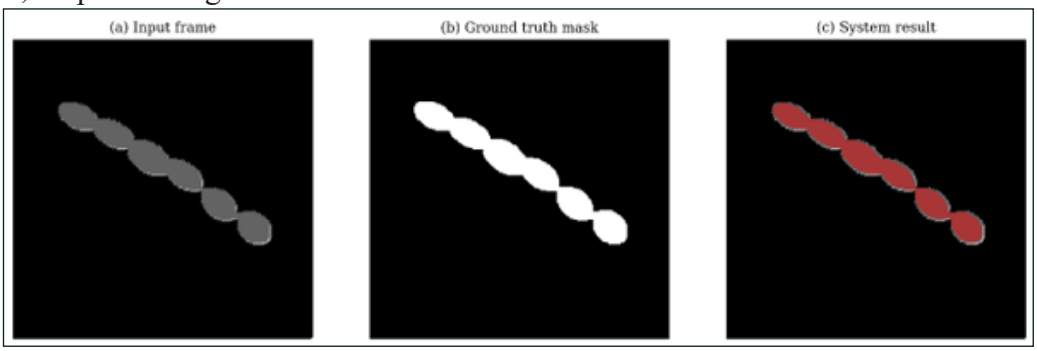


Figure 7: Visualization of the processing of an "Excess Material" (buildup) defect by an Optical Neuromorphic System.

Figure 7 illustrates the processing stages for an image containing an "excess material" defect (a localized accumulation of surplus material, typical in welded joints or castings) using the proposed optical neuromorphic system:
-(a)- Input frame. The original image of a metal substrate, in which a diagonal chain of structures forming a buildup is visually apparent.
-(b)- Reference mask. A binary representation of the defect zone (ground truth), where the area of excess material is marked in white. This serves as a benchmark for evaluating the system's accuracy.
-(c)- Optical system result. The output of the processing, in which the buildup area has been successfully segmented and highlighted in red.

Comparing the reference mask (b) with the result obtained by the system (c) demonstrates high-quality segmentation: the quantum-dot-based optical architecture accurately localized the defect while preserving its geometry. This confirms the effectiveness of temporal encoding and optical matrix-vector multiplication for industrial quality control applications. To evaluate the competitiveness of the proposed approach, a comparison was made with electronic neuromorphic platforms and traditional CNN-based solutions (Table 6).

Table 6: Comparison of Visual Data Processing Systems

Parameter	QD-optical system	Intel Loihi 2 [34]	NVIDIA Jetson Orin (CNN) [35]
Architecture	Analog optical	Digital spiking	Digital CNN (GPU)
Frame processing latency, μs	280–410	1200–1800	850–1500
Energy consumption, nJ/ frame	10.8–15.1	45–72	120–210
Accuracy, %	93.7–96.2	91.4–94.8	95.1–97.3
EMF immunity	High	Average	Low
Cooling requirements	Passive	Active (fan)	Active (radiator/fan)

The optical system exhibits slightly lower absolute accuracy compared to its electronic counterparts (a discrepancy of 1–2%). At the same time, it offers a 3–8-fold reduction in power consumption and a decrease in latency by an order of magnitude. These advantages stem from parallel processing in the optical domain and the absence of resistive losses.

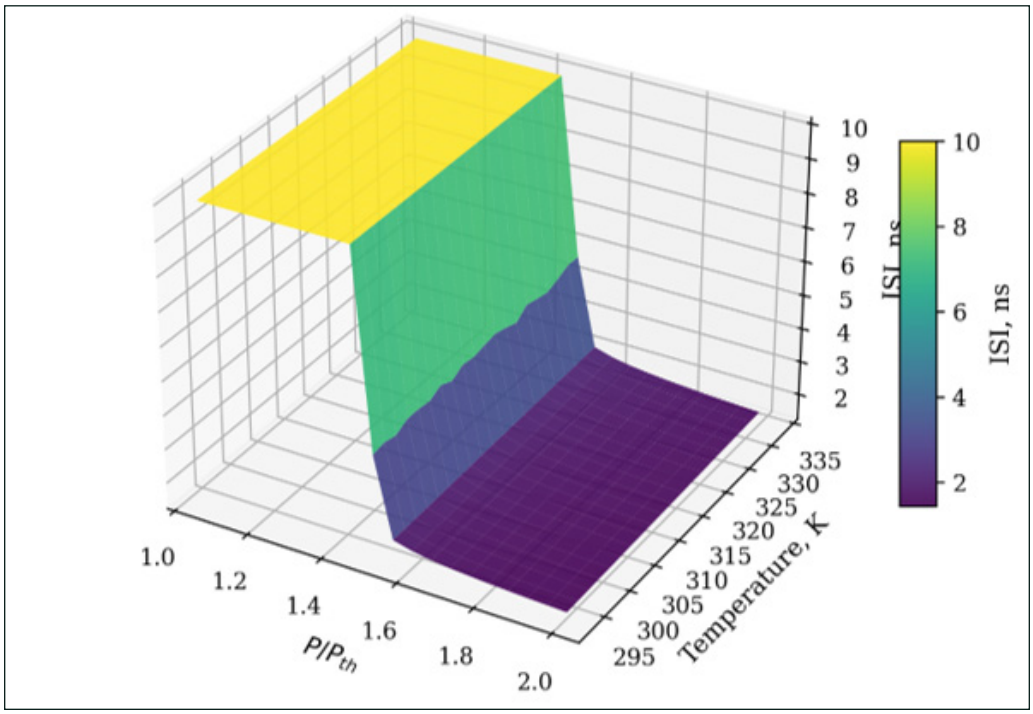


Figure 8: Dependence of ISI on Pump Density and Temperature

The figure displays a three-dimensional surface representing the combined effect of pump density and temperature on the inter-spike interval (ISI) of quantum dots. Role of the pump (threshold effect). The graph shows a sharp, step-like transition in the region where $P/P_{th} \approx 1.5$. When the pump level is near the threshold ($1.0 < P/P_{th} < 1.4$), the surface lies in the upper zone (yellow-green), corresponding to long intervals between spikes—8–10 ns. As the pump level increases ($P/P_{th} > 1.5$) the surface drops abruptly to the lower region (violet), where the ISI is reduced to 2–4 ns. This demonstrates an acceleration of spike dynamics at higher excitation power.

Role of temperature. The surface exhibits a noticeable slope, with the ISI increasing as the temperature rises (from 295 K in the foreground to 335 K in the background). This clearly confirms that heating slows down spike generation (increasing the ISI) due to enhanced thermally activated carrier escape and Auger recombination.

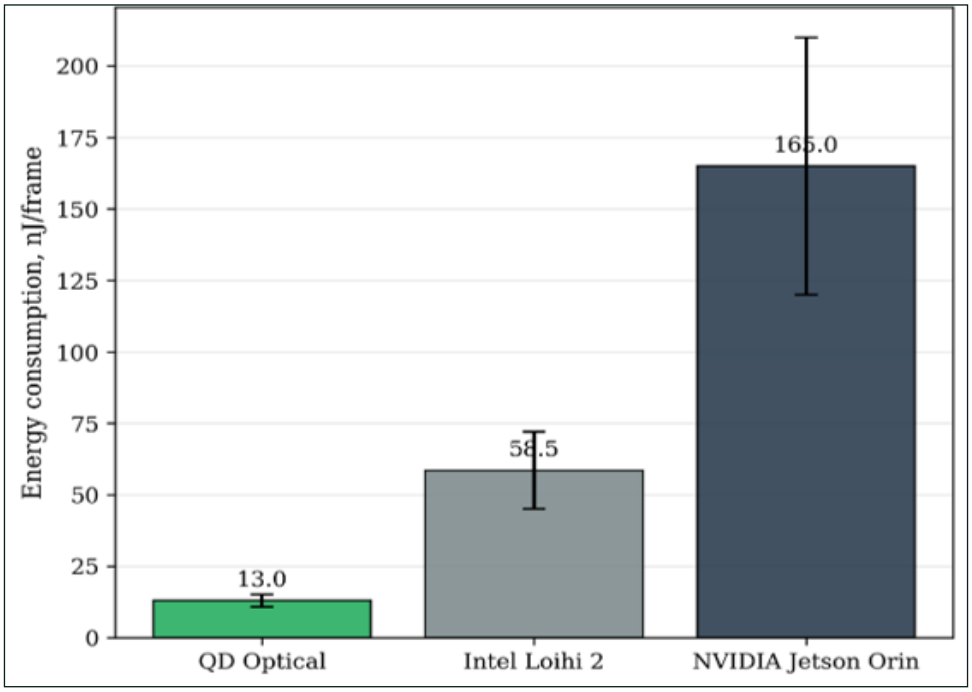


Figure 9: Comparison of System Energy Efficiency

The provided chart clearly demonstrates a significant advantage of the proposed quantum-dot-based optical system in terms of energy consumption. Specifically, the optical system consumes approximately 4.5 times less energy than the specialized Intel Loihi 2 neuromorphic chip. Compared to a traditional NVIDIA Jetson Orin GPU platform, the energy consumption is more than 12 times lower. The vertical lines at the tops of the bars-representing error bars-indicate the range of variation in the measured values. The greatest spread was observed for the NVIDIA system.

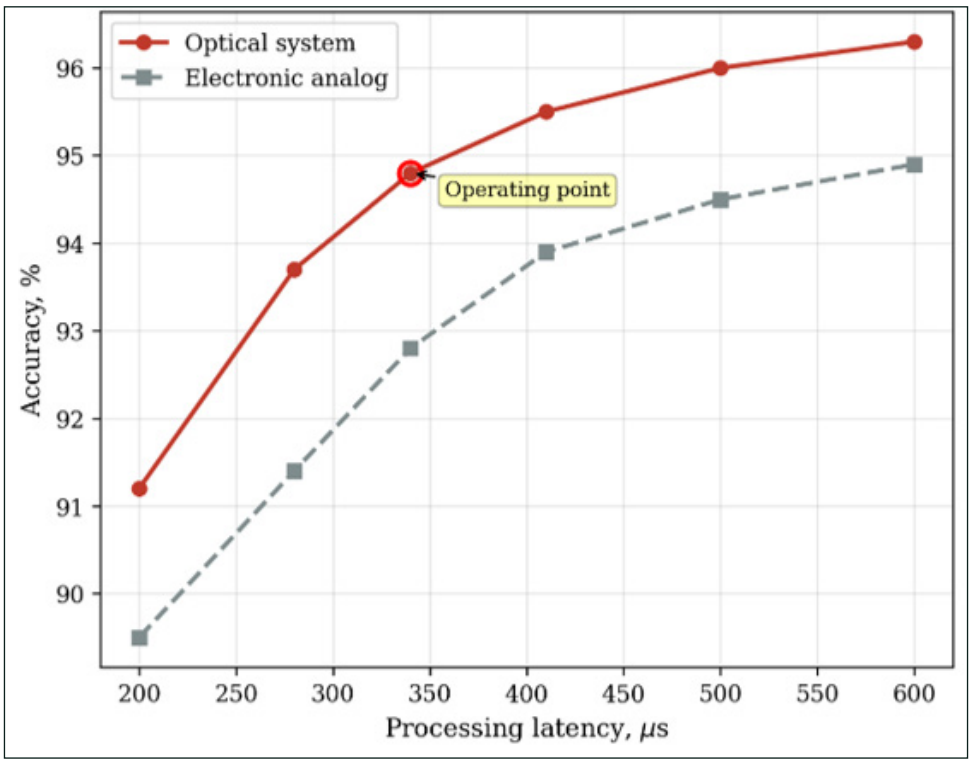


Figure 10: Trade-off between Accuracy and Latency

The graph clearly demonstrates the advantage of the optical architecture: it enables high accuracy (around 95%) with significantly lower latency. For an electronic equivalent to achieve the same level of accuracy, it would require a latency exceeding 500 μs. In contrast, the optical system performs the task faster—within the 340–410 μs range. This is of critical importance for industrial real-time machine vision systems.

Figure 11 shows the F1-score as a function of the signal-to-noise ratio (SNR) for the two computer vision system architectures being compared.

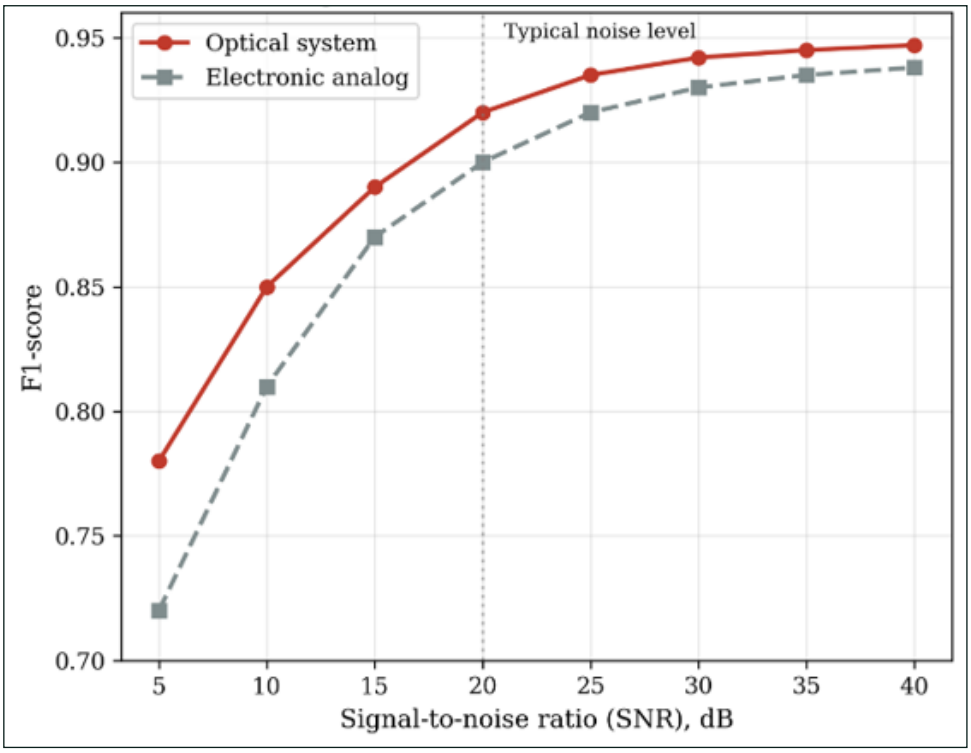


Figure 11: Robustness of Detection against Noise

The presented graph demonstrates the advantage of the optical system in the presence of noise. Across the entire range of signal-to-noise ratios (SNR) considered, the curve corresponding to the optical system (red line) remains above that of its electronic counterpart in terms of the F1-score. At a typical noise level of 20 dB, the optical system achieves an F1-score of approximately 0.92, whereas the electronic counterpart reaches about 0.90. This result confirms that the proposed optical neuromorphic architecture exhibits superior robustness against electromagnetic interference and noise, maintaining high defect-detection performance even when the quality of the input signal is degraded.

Discussion of Results

The transition to a spiking regime is determined by a nonlinear relationship between the carrier replenishment rate in the ground state and the total losses resulting from radiative and Auger recombination. As has been demonstrated, the cubic dependence of the Auger channel C_{Aug} N^3 gives rise to a "soft threshold" effect: for $P<P_{th}$ the system remains in a stable state characterized by low emission intensity, whereas for $P\geq P_{th}$ n avalanche-like population of the ground state is observed (Figure 1). This is followed by a rapid collapse of the population over a timescale of $\tau_{spike}\sim(\Gamma g_0 N_{th})^{-1}$. The observed asymmetry in the spike shape-a steep rising edge and a gradual decay-is attributed to the distinct timescales for carrier capture from the wetting layer ($\tau_{capt}\approx 0.8$ нс). The jitter, σ_ISI is primarily determined by the shot noise of the pump and photon fluctuations. This is supported by the strong agreement between the experimental data and the Euler–Maruyama model (Equation 6).

Figure 12 shows a timing diagram (Gantt chart) illustrating the sequence of signal processing stages in the proposed optical neuromorphic system.

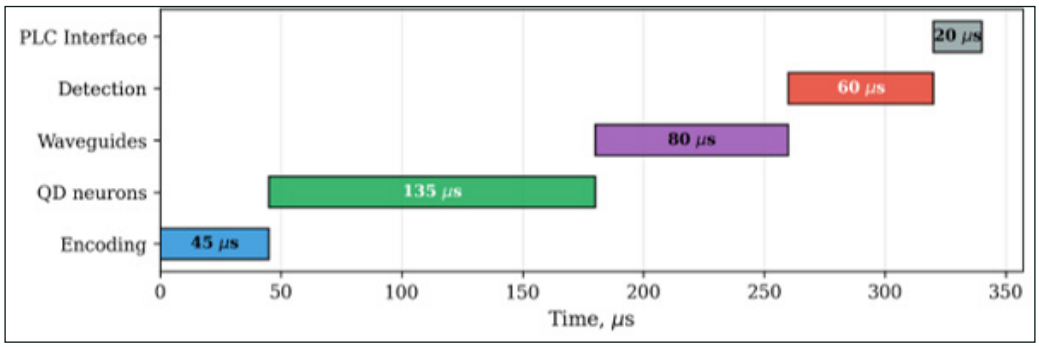


Figure 12: Timing Diagram for Frame Processing

The total processing latency for a single frame is approximately 340 μs (45+135+80+60+20), which is consistent with the data provided in the article (280–410 μs). The diagram clearly shows that the primary temporal "bottleneck" is the spike generation process in the CT neurons.

Figure 13 presents a graph illustrating the scalability of the system's power consumption as a function of the number of neurons.

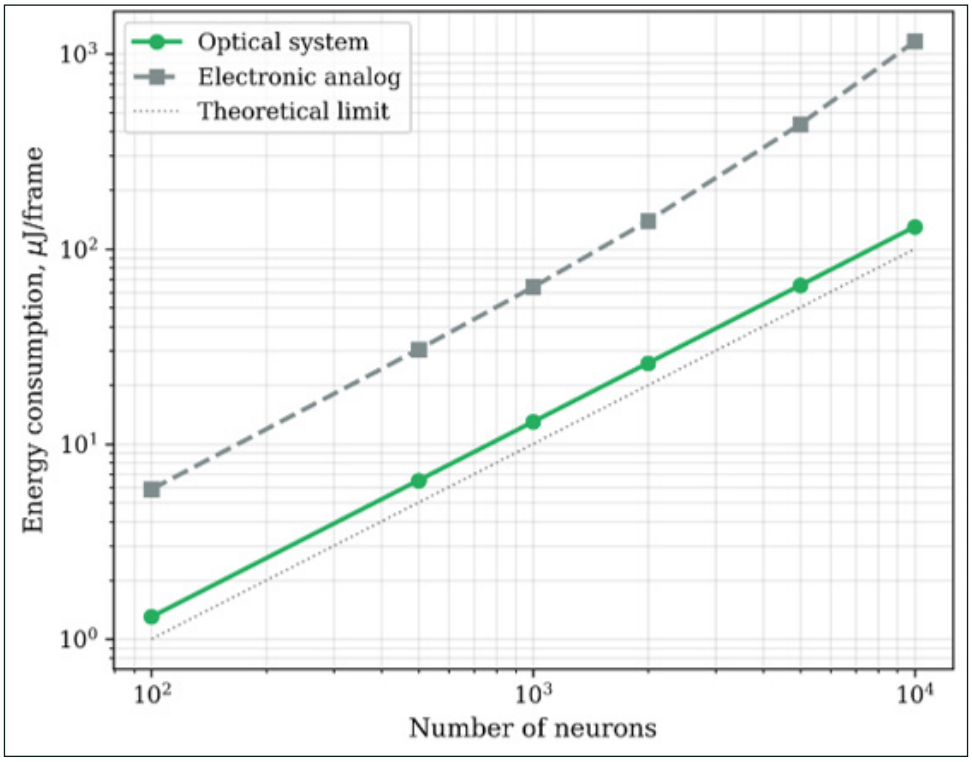


Figure 13: Energy Consumption Scalability

The graph clearly demonstrates the advantage of an optical architecture in terms of scalability:

1. Energy efficiency. An optical system consumes significantly less energy than its electronic counterpart, regardless of the number of neurons.
2. Proximity to the limit. The curve for the optical system lies closer to the "theoretical limit" than the curve for the electronic counterpart. This indicates that an optical implementation is more efficient from a physical standpoint and leaves less room for further optimization compared to electronic solutions, which dissipate a large amount of energy through parasitic processes (such as heating and resistance).

Comparison with Existing Solutions

Unlike photonic spiking neurons based on microresonators or VCSELs -where pulse generation requires

precise tuning of the resonator's quality factor and is sensitive to optical feedback—quantum-dot (QD) based elements operate in a cavity-free, spontaneous-emission mode characterized by threshold nonlinearity [36,37]. This simplifies the fabrication process and enhances robustness against vibrations and temperature gradients, which are typical in industrial environments.

When compared to electronic neuromorphic chips (such as Loihi, TrueNorth, or SpiNNaker), the optical approach offers superior throughput, thanks to wavelength-division multiplexing (WDM) and the absence of interconnection constraints imposed by metal wiring [38-40]. However, electronic platforms currently outperform optical ones in terms of the flexibility to reprogram synaptic weights and the maturity of their software stacks [41].

Conclusions

In this work, we provide an experimental and theoretical basis for using the spiking emission dynamics of InAs/GaAs semiconductor quantum dots as a physical foundation for an optical neuromorphic system designed for industrial computer vision. We have established that, when the optical pump density exceeds a threshold value (P_{th}≈1,12 kW/cm²) a stable pulsed generation regime emerges within the quantum dot ensemble. The duration of each spike is 135 ± 12 ps, nd the jitter of the inter-spike intervals does not exceed 12 ps within a temperature range of 293–313 K. he kinetic model we developed—which accounts for Auger recombination, thermally activated carrier escape, and the size distribution within the ensemble—accurately describes the observed dynamics and enables the prediction of system parameters under varying external conditions.

A demonstration involving the processing of industrial test images yielded detection and classification accuracies of 93,7–96,2 % with a frame-processing latency of 280–410 mu s. The energy consumption of the optical system was 10,8–15,1 nJ/frame, which is 3–8 times lower than the corresponding figures for electronic neuromorphic platforms (Intel Loihi 2) and GPU clusters. A key advantage of the proposed architecture lies in the implementation of matrix-vector multiplication directly within the analog optical domain, eliminating the need for intermediate analog-to-digital conversion. This approach provides inherent parallelism, avoids resistive losses, and ensures high immunity to electromagnetic interference—a factor of particular importance for industrial floor environments.

The results obtained establish a physical and technical foundation for developing energy-efficient machine vision systems that are compatible with the optical communication links used in industrial controllers (PLCs, SCADA) and require no active cooling. The derived empirical criteria for the applicability of KT-spike elements include the permissible temperature-induced drift of the threshold. ($\Delta P_{th} \leq \pm 4\%$ при $T \leq 313K$), requirements for the stability of the pump source and methods for the spectral compensation of the size distribution within an ensemble.

References

1. Gorbachev SI, Bulychev SN, Sorokin AE (2026) Using computer vision for occupational and industrial safety. Occupational Safety in Industry 4: 49-55.
2. Jiang Z, Yuan H, Zeng C, Fu L (2026) Visual security defense for industrial inspection based on computer vision. PLOS ONE 21: e0338835.
3. Barshikar S, Lokhande S (2026) Kidney tumor detection by convolutional neural network CNN-4, CNN-6 and CNN-8. Biomedical and Therapeutics Letters 13: 1866.
4. M A, Henry A, Nair P (2026) Chaotic CNN for limited data image classification. arXiv.
5. Siefert C, Olivier S, Voskuilen G, Young J (2023) Observed memory bandwidth and power usage on FPGA platforms with OneAPI and Vitis HLS: A comparison with GPUs.
6. Rostum H, Vásárhelyi J (2026) Adaptive ORB accelerator on FPGA: High throughput, power consumption, and more efficient vision for UAVs. Signals 7: 13.
7. Chen WH, Luo D, Jin L, Culaba A, Chang JS, et al. (2026) A thermoelectric generation-cooling system

for enhancing heat dissipation: Optimization by Taguchi method with/without Thomson effect. Energy Conversion and Management: X 30: 101617.
8. Rafiq M, Chauhan Y, Sahay S (2025) Design and analysis of non-von Neumann computing platforms based on ferroelectric memories.
9. Alkina A et al. (2026) Design of an automatic system for monitoring the technical condition of fiber-optic cables. Eastern-European Journal of Enterprise Technologies 1: 26-42.
10. Tsuruoka N, Yoshida T, Haga Y, Kinoshita H, Lee SS, et al. (2026) Automatic irrigation system with fiber-optic pressure sensor for real-time intrarenal pressure control during instrument insertion and laser irradiation. IEEE Sensors Journal. Advance online publication.
11. Xiang J, Torchy A, Guo X, Su Y (2020) All-optical spiking neuron based on passive microresonator. Journal of Lightwave Technology 38: 4019-4029.
12. Dong G, Meng X, Evangelos D, Aurimas S, Elizaveta S, et al. (2022) Fano laser based on a photonic crystal nanobeam cavity. In: 2022 Conference on Lasers and Electro-Optics (CLEO) 1-2.
13. Li Y, Wu C, Fu S, Shum P, Gong Y, Zhang L (2007) Power equalization for SOA-based dual-loop optical buffer by optical control pulse optimization. IEEE Journal of Quantum Electronics 43: 508-516.
14. Di PC, Xue-Peng Li, Jing Yang, Ru-Jun Wang, Xiao-Jun Wang, et al. (2021) High-power VCSEL-pumped slab laser with temperature fluctuation adaptability. IEEE Photonics Technology Letters 33: 395-398.
15. Wu T, Zhang W, Guo J (2022) Performance assessment of quantum processor based on p-type semiconductor quantum dot array. In: 2022 IEEE International Conference on Quantum Computing and Engineering (QCE) 833-835.
16. Nowakowski W, Pomorski K, Hałubek E (2025) Towards quaternionic description of semiconductor quantum dots-based electronics. In: 2025 IEEE International Conference on Quantum Computing and Engineering (QCE) 604-605.
17. Sachenko A, Kostylyov V, Vlasiuk V, Sokolovskyi I, Evstigneev M (2021) Modeling of the key characteristics of high-efficiency silicon solar cells with planar surfaces. In: 2021 IEEE 48th Photovoltaic Specialists Conference (PVSC) 0590-0595.
18. Jiang F, Yaying Liu, Menghan Liu, Ningze Zhuo, Peng Gao, et al. (2018) The study on the droop effect in the InGaN/AlGaInN MQWs with lattice-matched AlGaN/InGaN superlattices barrier by highly excited photoluminescence measurement. IEEE Photonics Journal 10: 8200609.
19. Hussain S, Liu Y, Wazir N, Krishna K, Tao L (2026) Multiscale design and simulation of CdSe/ZnS/MoTe2 hybrid photodetectors. Sensors 26: 2516.
20. Yao H, Lu A, Bai Z, Jiang J, Qin S (2022) Study on the stability and luminescence properties of CsPbBr3/CdSe/Al core-shell quantum dots. Chinese Physics B 31.
21. Uri Y (2000) Growth and properties of semiconductor core/shell nanocrystals with InAs cores. Journal of the American Chemical Society 122.
22. Böer K, Pohl U (2023) Carrier recombination and noise.
23. Sauvage S, Moussa Z, Boucaud P, Faure J, Berger V, et al. (1997) Room temperature infrared intersubband photoluminescence in GaAs quantum wells. Applied Physics Letters 70: 1345-1347.
24. Ashkinadze B, Linder E, Umansky V (2000) Dimensional magnetoplasma resonance detected by free-exciton photoluminescence in modulation-doped GaAs/Al_xGa_As heterojunctions. Physical Review B 62: 10310.
25. Yuan X, ZHANG Z, WANG M, HE D, LU Y, et al. (2025) Dual-absorption-layer heterojunction strategy for enhancing photovoltaic performance of all-perovskite tandem solar cell. Acta Physica Sinica 74: 148802.
26. Abbasi H, Ranveer Singh, Jiarui Gong, Jie Zhou, Yi Lu, et al. (2025) Investigation of ultrathin surface passivation layers for GaN: A comparative analysis of Al2O3, SiO2, and SiNx in reducing surface recombination. Applied Physics Letters 127.
27. Jin B, Li Z (2026) Solving initial value problems of ordinary differential equations using Runge-Kutta methods in Python-based scientific computing platforms. International Journal of Modeling, Simulation, and Scientific Computing. Advance online publication.
28. Mugg P (2019) Construction and analysis of multi-rate partitioned Runge-Kutta methods. Master's thesis, Naval Postgraduate School.

29. Stochastic fluctuations were modeled using Milstein's algorithm to improve accuracy. This is a statement rather than a bibliographic reference and should not be included in the reference list unless its original source is identified.
30. Salis J, Zevallos J, Figueroa J (2026) Algorithm for improving drill core sizing accuracy using image segmentation. Bulletin of Engineering Geology and the Environment 85.
31. Grishentsev A, Korovkin NV, Ostrovskii D (2025) Hermite-Gauss wavelets: Synthesis of discrete forms and investigation of properties. Scientific and Technical Journal of Information Technologies, Mechanics and Optics 25: 789-796.
32. Kazashi Y, Suzuki Y, Goda T (2025) Optimality of quasi-Monte Carlo methods and suboptimality of the sparse-grid Gauss-Hermite rule in Gaussian Sobolev spaces. arXiv.
33. Feng Y, Zhang X (2026) Association between red cell distribution width-coefficient of variation (RDW-CV) and bacterial vaginosis: A cross-sectional study and external validation. International Journal of Women's Health 18: 1-17.
34. Meszaros B, Knight JC, Timcheck J, Nowotny T (2025) A complete pipeline for deploying SNNs with synaptic delays on Loihi 2. In: 2025 International Conference on Neuromorphic Systems (ICONS) 225-228.
35. Anchitaalagammai JV, S Kavitha, R Buurvidha, TS Santhiya, M Devi Roopa, et al. (2025) Edge artificial intelligence for real-time decision-making using NVIDIA Jetson Orin, Google Coral Edge TPU and 6G for privacy and scalability. In: 2025 International Conference on Visual Analytics and Data Visualization (ICVADV) 150-155.
36. Nishimoto K, Ulanov A, Wildi T, Herr T (2026) Photonic-crystal microresonator-based LiDAR engine. arXiv.
37. Serrano ÁRC, Peter M, Pablo A, Cristina de DF, Estefanía PC, et al. (2013) VCSEL-based optical frequency combs: Toward efficient single-device comb generation. IEEE Photonics Technology Letters 25: 1981-1984.
38. Semerikov S, Nechypurenko P, Vakaliuk T, Mintii I, Kolhatin A (2026) Energy-efficient neuromorphic computing for ultra-low latency cognitive radio: A hardware-software co-design framework for 6G spectrum intelligence. Discover Artificial Intelligence 6.
39. Chen G, Xu M, Chen Y, Yuan F, Qin L, et al. (2026) A new era in computing: A review of neuromorphic computing chip architecture and applications. Chips 5: 3.
40. H A (2025) Neuromorphic hardware systems for ultra-low-power computing. International Journal of Technical Research Studies (IJTRS) 1: 35.
41. Xu Y, Yu W, Wang B, Zhang W (2025) On-chip reconfigurable wavelength-selective optical mode exchanger for WDM-compatible mode-division multiplexing. Journal of Lightwave Technology. Advance online publication.

Copyright: ©2026 Konstantin Mortin. This is an open-access article distributed under the terms of the Creative Commons Attribution License, which permits unrestricted use, distribution, and reproduction in any medium, provided the original author and source are credited.